RMetS
Royal Meteorological Society

Moisture transport in midlatitude cyclones

I. A. Boutle,* S. E. Belcher and R. S. Plant
Department of Meteorology, University of Reading, Reading, UK
*Correspondence to: I. A. Boutle, Met Office, FitzRoy Road, Exeter, EX1 3PB, UK.
E-mail: ian.boutle@metoffice.gov.uk

We discuss how synoptic-scale variability controls the transport of atmospheric water vapour by midlatitude cyclones. Idealized simulations are used to investigate quantitatively which factors determine the magnitude of cyclone moisture transport. It is demonstrated that large-scale ascent on the warm conveyor belt and shallow cumulus convection are equally important for ventilating moisture from the boundary layer into the free troposphere, and that ventilated moisture can be transported large distances eastwards and polewards by the cyclone, before being returned to the surface as precipitation.

The initial relative humidity is shown to have little effect on the ability of the cyclone to transport moisture, whilst the absolute temperature and meridional temperature gradient provide much stronger controls. Scaling arguments are presented to quantify the dependence of moisture transport on large-scale and boundary-layer parameters. It is shown that ventilation by shallow convection and warm-conveyor-belt advection vary in the same way with changes to large-scale parameters. However, shallow convective ventilation has a much stronger dependence on boundary-layer parameters than warm-conveyor-belt ventilation.

Key Words: warm conveyor belts; convection; boundary-layer ventilation; water cycle

Received 21 July 2010; Revised 9 December 2010; Accepted 4 January 2011; Published online in Wiley Online Library

Citation: Boutle IA, Belcher SE, Plant RS. 2011. Moisture transport in midlatitude cyclones. *Q. J. R. Meteorol. Soc.* **137**: 360–373. DOI:10.1002/qj.783

1. Introduction

The pattern of water vapour in the troposphere is shaped by processes on a wide variety of scales, from evaporation at the surface, through boundary-layer mixing and convection, synoptic- and global-scale motions, to precipitation back to the surface. Schneider *et al.* (2006) developed a climatology of the zonal-mean structure of tropospheric water vapour and the zonal-mean fluxes that shape this pattern. In general terms, the sources of water vapour are at the surface in the tropics and subtropics. Synoptic-scale eddies then flux this water vapour into the upper troposphere in the extratropics. Furthermore, Trenberth and Stepaniak (2003) demonstrate that this latent energy transport accounts for approximately half of the atmospheric energy flux in the midlatitudes. A striking conclusion of these studies is that the poleward moisture flux, carried mainly by synoptic-scale eddies, not only determines the precipitation distribution but also plays a significant role in shaping the temperature structure of the planet. This raises the question of how transport is achieved on the scale of an individual weather system.

A recent article by Boutle *et al.* (2010) has investigated the boundary-layer structure and low-level moisture transport in an idealized, numerically simulated baroclinic wave. Boundary-layer budgeting techniques were used to quantify evaporation, transport within and ventilation of moisture from the boundary layer. It was shown that large-scale ventilation on the warm conveyor belt (WCB) was of similar importance to shallow convective ventilation in cumulus clouds, demonstrating that both processes play an important role in the vertical transport of moisture from the surface into the free troposphere. However, they did not investigate

how moisture was transported zonally or meridionally within the free troposphere. WCBs are often considered to be the primary mechanism for tropospheric transport by cyclones (Wernli, 1997; Eckhardt *et al.*, 2004), but what factors control the moisture transport by WCBs? Similarly, if convective processes are important for ventilating moisture from the boundary layer, what happens to the moisture once it is ventilated and what factors control this moisture transport?

Quantifying cyclone moisture transport can help us to understand the role larger-scale processes play in shaping the global water cycle. For example, the North Atlantic Oscillation (NAO) is known to exert a strong control over the midlatitude jet, causing variations in its strength and orientation which, in turn, exert a control over the strength and location of midlatitude cyclones. Stohl *et al.* (2008) demonstrated that in a positive phase of the NAO, characterized by a stronger midlatitude jet, subtropical sources of moisture are important for heavy rainfall events in mid to high latitudes. Ruprecht *et al.* (2002) also demonstrated higher polewards moisture transport in a positive phase of the NAO, linked to more intense cyclones producing the transport. They also showed that the location of maximum moisture transport was shifted further north in a positive NAO, linked to a poleward shift of the jet under positive NAO conditions. Whilst these studies provide qualitative evidence for the link between jet strength and moisture transport, they do not quantify how moisture transport can be expected to change with a given change in jet strength.

There are also important climatological questions that can be answered by investigating cyclone moisture transport. Recent articles by Field and Wood (2007) and Field *et al.* (2008) have discussed the structure of cyclones in a composite of both real-world events and climate-model simulations. They discussed how the cyclone-averaged near-surface wind speed $\langle V \rangle$ and water-vapour path $\langle WVP \rangle$ could be used as independent metrics of cyclone intensity and moisture availability to explain a considerable amount of observed variability. They showed how the WCB rain rate was proportional to the product of these two metrics, and that $\langle WVP \rangle$ increased with increasing sea-surface temperature (SST) according to the Clausius–Clapeyron equation. They also discussed the implications of their results on the way cyclones may change in a warming climate. Allen and Ingram (2002) discuss how the Clausius–Clapeyron equation should give a $6.5\%\,\mathrm{K}^{-1}$ increase in global atmospheric water-vapour storage, but the total global precipitation should only increase at $2\%\,\mathrm{K}^{-1}$, constrained by the global energy balance. Hence Field and Wood (2007) and Field *et al.* (2008) suggested that cyclones should be fewer in number or less intense to account for this difference, effects that have both been seen in modelling studies (Meehl *et al.*, 2007; Bengtsson *et al.*, 2006), but it is presently unclear which process is more likely. Could the necessary adjustment be achieved through changes in the jet?

This article aims to address the questions raised above, focusing on an individual baroclinic system to determine the controls on the cycling of water vapour through the system. We aim to quantify the dominant controls on moisture transport from large-scale and convective motions, and to establish a scaling for these processes. Section 2 introduces the idealized model used, with section 3 describing the moisture cycle in the control simulation. In section 4 we investigate how changes to large-scale parameters influence the moisture cycle. In section 4.1, changes to the initial relative humidity distribution are investigated, demonstrating why the idea that relative humidity remains approximately constant (Allen and Ingram, 2002; Field and Wood, 2007) works for baroclinic waves. Section 4.2 investigates the effect of the absolute atmospheric temperature on the cyclone moisture cycle, with section 4.3 considering the effect of the meridional temperature gradient. Scaling arguments for how these large-scale changes affect both advective and convective moisture ventilation from the boundary layer are given in section 5. Section 6 then discusses how changes to the boundary-layer structure can have markedly different effects on the two ventilation processes, before conclusions are drawn in section 7.

2. Model description

The control simulation used in this article is the same as that used in Boutle *et al.* (2010), who presented an idealized baroclinic-wave simulation similar to that denoted LC1 by Thorncroft *et al.* (1993). The Met Office Unified Model (MetUM) is used in idealized mode, allowing us to use its full range of physical parametrizations to model turbulent and moist atmospheric processes. The MetUM employs a semi-Lagrangian advection scheme, with semi-implicit time integration. For this study, the dynamics are coupled to physical parametrizations of boundary-layer turbulence, shallow and deep convection, mixed-phase microphysics and large-scale cloud. These dynamics and physics schemes are similar to those used in the operational global forecast model and the HadGEM1 climate model, and full details of the schemes can be found in Martin *et al.* (2006) and references therein. The model is configured on a limited-area domain of 60° longitude by 80° latitude, at 0.4° horizontal resolution and with 38 staggered vertical levels below 40 km, giving the finest resolution near the surface. East–west periodic boundary conditions are applied, giving wavenumber-6 symmetry to our simulations.

The large meridional extent is chosen in order that the north–south boundaries do not affect the simulations. The model is also configured on a Cartesian f-plane. This choice is made as we wish to vary the Coriolis parameter to determine its influence on moisture transport, and the use of a Cartesian f-plane ensures that the size of cyclone does not change and therefore the area over which ventilation occurs is unaffected. The differences between cyclones in spherical and Cartesian geometry are well documented in the literature (Balasubramanian and Garner, 1997; Wernli *et al.*, 1998), with the main difference being that Cartesian simulations tend to be more cyclonic in nature. The addition of a barotropic cyclonic shear to a spherical simulation leads to a simulation very similar to our Cartesian one. Furthermore, Wernli *et al.* (1998) describe how this Cartesian simulation is similar to the conceptual model of Shapiro and Keyser (1990), with a T-bone frontal structure developing and a bent-back warm front wrapping around the low centre.

The initialization follows that of Polvani and Esler (2007) to specify the initial-condition wind field analytically as

$$u(\phi, z) = U_0 \sin^3[\pi \sin^2(\phi)] \frac{z}{z_T} \exp\left(-\frac{(z/z_T)^2 - 1}{2}\right), \quad (1)$$

where ϕ is the latitude, z is the height, $U_0 = 45\,\mathrm{m\,s^{-1}}$ is the maximum jet speed and $z_T = 13\,\mathrm{km}$ is the temperature scale height. A temperature profile in thermal wind balance with this is then constructed, integrated from a vertical profile of constant static stability ($4\,\mathrm{K\,km^{-1}}$ below z_T, $16\,\mathrm{K\,km^{-1}}$ above) and surface temperature of $T_0 = 280\,\mathrm{K}$ at 45°N (the jet centre). A pressure profile is constructed in hydrostatic balance, and the model is run for several time steps to allow the wind, temperature and pressure fields to adjust to the nonlinear balance consistent with the equation set of the MetUM. The moisture field is initialized in terms of relative humidity (RH) as

$$RH(\phi, z) = \begin{cases} RH_0[1 - 0.9R(\phi)(z/z_q)^{5/4}] & z < z_q, \\ RH_0(0.0625) & z > z_q, \end{cases} \quad (2)$$

where $RH_0 = 80\%$, $z_q = 12\,\mathrm{km}$ and $R(\phi)$ defines the latitudinal variation of RH as given in Boutle *et al.* (2010). The sea-surface temperature is fixed throughout the simulation and equal to the initial temperature of the lowest model level. The jet structure is baroclinically unstable, and so a small perturbation, given in Polvani and Esler (2007), is added to the temperature field to trigger cyclogenesis.

The simulations are run for 14 days, over which time an alternating series of high- and low-pressure systems forms and intensifies. The system undergoes periods of linear and nonlinear growth, reaching its peak intensity between days 10 and 11 before starting to decay. The spatial structure of the surface pressure, fronts, cloud fraction and precipitation rate at days 7 and 9 is shown in Figure 1. It shows many features of a typical midlatitude weather system, such as the main precipitation band located in the WCB. This poleward airstream of warm, moist air runs ahead of the cold front and ascends over the warm front. It splits into two branches; one turns cyclonically and wraps around the north of the low centre, whilst the other turns anticyclonically east towards the neighbouring high pressure. Also noticeable in Figure 1 is some cloud-free air south of the low centre, immediately behind the cold front. This is associated with the descending air in the dry intrusion. Further behind the cold front and to the west of the cyclone centre are low-level cumulus clouds. These are formed in a cold-air outbreak, as shallow convection is triggered by cold air flowing from the north over a warmer sea surface.

3. Moisture cycle of a baroclinic wave

Boutle *et al.* (2010) discussed how moisture, evaporated from the sea surface, was transported through the atmospheric boundary layer and ventilated into the troposphere in two main regions. Their results are summarized schematically in Figure 2. Moisture is evaporated from the sea surface behind the cold front and in the high-pressure part of the wave. Approximately half of this moisture is locally ventilated from the boundary layer in shallow convection in cumulus clouds above the region of positive surface fluxes. The rest of the moisture is transported within the boundary layer by divergent and convergent motions, forced by surface drag and large-scale ageostrophic motions. The moisture converges into the footprint of the WCB. Here the surface fluxes are negative and a small amount of moisture is returned to the surface. However, most of the moisture is ventilated from the boundary layer by large-scale ascent on the WCB. Therefore, the cyclone boundary layer is capable of taking moisture from a single source region and processing it through two separate ventilation regions.

Figure 3 shows a time series of boundary-layer ventilation from these two processes over the life cycle. The WCB ventilation is calculated as the moisture flux through the boundary-layer top in the WCB area. Here, the WCB area is defined using the method of Sinclair *et al.* (2008), which locates the 95th percentile of the entire vertical velocity on boundary-layer top dataset and defines the WCB as any ascent greater than this value. Sinclair *et al.* (2008) demonstrated that this definition finds the majority of the WCB, rather than just the core. Increasing the percentile would result in only part of the WCB ventilation being observed, whereas reducing the percentile leads to the inclusion of areas that are not part of the WCB. The convective ventilation is calculated directly from the moisture flux parametrized by the convection scheme, summed over all points on which the convection scheme is active. Both processes start ventilating around day 4, with shallow convection ventilating at a slightly faster rate than the WCB up to day 8. The shallow convective ventilation peaks at day 10 before decaying, whilst the WCB ventilation continues to day 11, coincident with the peak eddy kinetic energy (EKE) of the simulation. The WCB ventilation also peaks approximately 20% higher than the convective ventilation before starting to decay at a similar rate. This increased peak means that, over the life cycle, the WCB ventilates $\approx$ 10% more moisture than the shallow convection.

Figure 3 also shows the precipitation rate from the WCB. Here, we define the WCB precipitation as that produced by the large-scale ascent of the WCB, ensuring that we track the large-scale moisture flow responsible for boundary-layer ventilation by the WCB. There is some additional convective precipitation not included in this measure, although this is mainly confined to the cold front. As shown, the precipitation rate closely matches the WCB ventilation rate, demonstrating that WCBs are approximately 100% efficient at converting moisture into precipitation. This fact is also demonstrated by Eckhardt *et al.* (2004) for a climatology study of many WCBs. There is no time lag in this process, due to the presence of a background moisture profile. As soon as ascent starts (around day 3), some moisture present within the troposphere is forced to ascend past its lifting condensation level, condensing into cloud and precipitating. At the same time, moisture is ventilated from the boundary layer to replace the moisture lost from the troposphere. Hence the conveyor-belt analogy is a good one, as moisture is 'loaded' on to the conveyor belt at one end (in the boundary layer) whilst microphysical processes remove moisture at the other end (in the troposphere) at approximately the same rate. The total moisture content of the troposphere is largely unchanged by this process, although its spatial distribution is. Since the WCB also flows polewards, atmospheric water vapour is moved polewards by the WCB. Hence the WCB forms part of the cyclone's

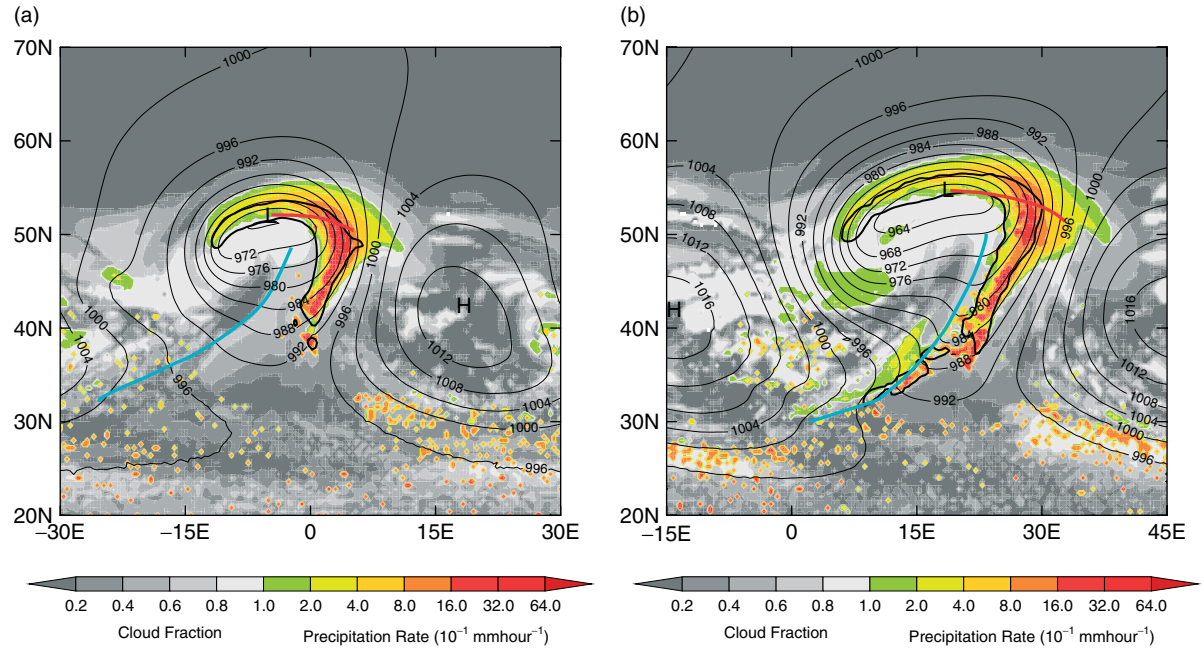

Figure 1. Cloud fraction (shaded) and precipitation rate (coloured), with pressure at mean sea level (contoured, interval 4 hPa) at (a) day 7 and (b) day 9. Also shown are the warm (red) and cold (blue) fronts and the extent of the warm conveyor belt footprint area (black).

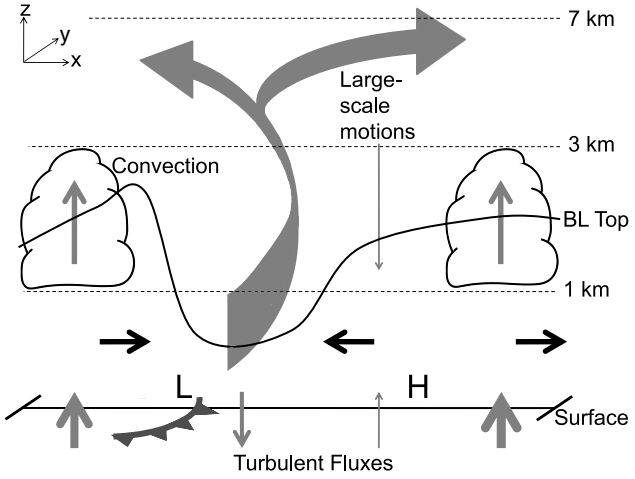

Figure 2. Schematic representing the flows of moisture within the cyclone boundary layer. Grey arrows represent sources and sinks of boundary-layer moisture and black arrows represent advection within the boundary layer. The arrow thickness provides a qualitative indication of the relative strength of the various flows. L and H denote the low- and high-pressure centres respectively, with the cold front also marked. The approximate height of features is marked, along with the height of the boundary layer.

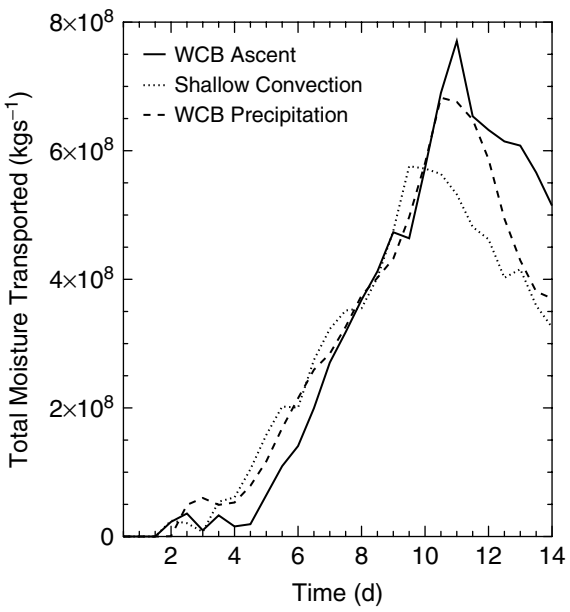

Figure 3. Time series of total moisture ventilated from the boundary layer by warm conveyor belt ascent (solid) and shallow convection (dotted). Also shown is the surface precipitation rate from the warm conveyor belt (dashed).

ability to transport large amounts of water vapour for long distances polewards, as discussed by Stohl *et al.* (2008).

Attention is now focused on the moisture ventilated by shallow convection. To ascertain how this moisture is transported by the cyclone, a tracer study has been performed. A passive tracer is emitted at the surface continually throughout the life cycle. It is massless and acts simply as a tracer to track airflows within the cyclone. The advantage of a tracer study is that it does not alter the model evolution, but different tracers can be passed through different parametrization schemes, demonstrating the importance of different physical processes on tracer transport. Two tracers are emitted at the same rate from the surface, both of which are advected by the resolved winds and mixed vertically by the parametrized turbulence. However, the first tracer is transported vertically by the parametrized convection whilst the second tracer is not. Therefore the difference between the two tracers represents the action of convection on the tracer concentrations. The tracer transport can be used as a proxy for moisture transport by convection because the convection occurs over regions of large, positive surface latent heat fluxes, and so the continual tracer source from the surface represents the moisture source. Figure 1 shows that there is limited precipitation in the convective regions, which will remove some moisture, but the tracer is representative of what will happen to any moisture that is not instantaneously precipitated.

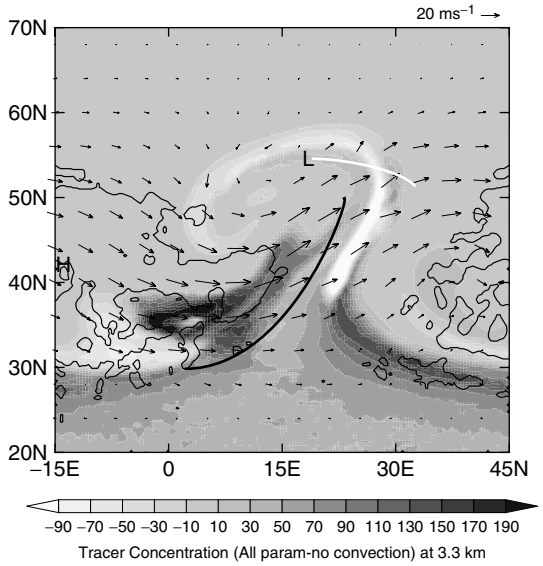

Figure 4. Tracer concentration (arbitrary units) ventilated by convection at 3.3 km (shading), with wind vectors at 3.3 km overplotted, at day 9. Regions of cumulus-capped boundary layers are marked by thin black lines, with the warm/cold fronts also shown by thick white/black lines.

Figure 4 shows the distribution of this tracer difference at day 9 at the approximate height of the convective cloud tops. The figure shows a large increase in tracer behind the cold front, in the region 0–15°E, 30–40°N, which is tracer-ventilated by shallow convection. It is noticeable that this tracer is no longer located in the region of cumulus-capped boundary layer, but has been advected eastwards by the jet towards the cold front. This is consistent with the results of Gutowski and Jiang (1998), who demonstrated that tracers released near convective cloud tops can be transported eastwards and polewards over several days towards the cold front. The poleward motion of these tracers is noticeable around 15°E, 45°N as a tongue of high tracer concentration extends towards the low centre. This tracer therefore demonstrates how moisture ventilated by shallow convection is transported eastwards and polewards (in a system-relative sense) within the troposphere, towards the cyclone cold front. Comparison with Figure 1(b) shows that some of this moisture is precipitated back to the surface in showers located within the cold-air outbreak. The remaining moisture must eventually return to the surface as precipitation, since over the whole life cycle precipitation approximately balances evaporation, and this precipitation is likely to occur on the cold front.

Balasubramanian and Garner (1997) discussed how these idealized cyclones remain confined within the latitude band of the initial zonal jet, particularly in Cartesian simulations. However, in reality cyclones are known to migrate polewards, especially in the North Atlantic where the jet orientation is typically southwest–northeast. It has been demonstrated that moisture is transported polewards in a system-relative sense and therefore if the system is also migrating significantly polewards then the poleward moisture transport will be enhanced. Therefore, convective processes are a significant contributor to the poleward moisture transport by midlatitude cyclones.

Figure 4 also shows a large decrease in tracer in the WCB region (20–30°E, 40–50°N). There is also a decrease in tracer concentrations near the high-pressure centre, around −10°E, 35°N, which is part of the anticyclonic branch of the WCB that has descended under large-scale subsidence. This implies that the concentrations in these regions are higher for a tracer not subject to convective processes. Therefore, it appears that the convection is reducing the ability of the WCB to ventilate the tracer. Since convection removes the tracer from the post-frontal regions on a time-scale of hours, there is less tracer in these regions to be transported within the boundary layer by divergent motions. Therefore, less tracer converges into the WCB footprint and less is available for ventilation. When the tracer cannot be ventilated by shallow convection, it accumulates in the boundary layer and is transported and ventilated by large-scale processes. Moist convection acts as a limiting process on tracer ventilation by the WCB.

The results suggest that if there were no convection then, as happened with the tracer, more moisture could be ventilated by the WCB, ultimately enhancing WCB precipitation rates. In reality, convection cannot simply be turned off. However, the results do have consequences for numerical weather prediction and climate simulations. The convection parametrization is not perfect, and different models use different convection parametrizations that could ventilate different amounts of moisture. Whilst it is beyond the scope of this study to investigate the sensitivity of the convective ventilation to the parametrization used, the tracer study demonstrates that any differences in the convective ventilation could feed back on to large scales. Therefore, it is possible that two different convection schemes ventilating different amounts of moisture could lead to changes in the large-scale ventilation and WCB precipitation. The moisture ventilated is not a passive tracer, but will feedback on to the cyclone evolution through latent-heat release, possibly intensifying the system and further increasing WCB precipitation.

The boundary layer therefore plays an important role in the moisture cycle of a baroclinic wave. Surface evaporation provides a source of moisture to the boundary layer. Fast convective processes are able to remove large amounts of moisture from the boundary layer, which is transported eastwards and polewards by the cyclone system. The convection also regulates the amount of moisture that is available to be transported by slower, large-scale processes within the boundary layer. Ultimately, this affects the ventilation rate by the WCB and the precipitation delivered by the cyclone.

4. Large-scale controls

This section will investigate how changes to the large-scale atmospheric state, i.e. the initial conditions for the idealized simulations, control the moisture ventilation from the boundary layer. A metric of boundary-layer moisture ventilation has been constructed, given by

$$Q = \int_{\mathcal{T}} \int_{A} (\rho q)_h w_h \, \mathrm{d}A \, \mathrm{d}t, \tag{3}$$

where Q is the total mass of moisture ventilated by the process of interest, $\mathcal{T} = 14$ days is the time of a single life cycle, A is the area over which ventilation occurs, ρ is the density of air, q is the specific humidity, w is the vertical velocity and the subscript h denotes a quantity evaluated at the boundary-layer top. Motivated by section 3, ventilation by WCB advection (denoted Q_{wcb}) and shallow convection

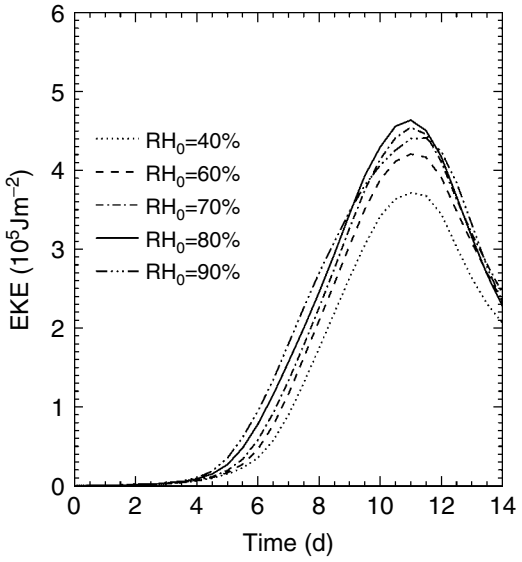

Figure 5. Time series of eddy kinetic energy for various values of the initial surface RH (shown on the plot).

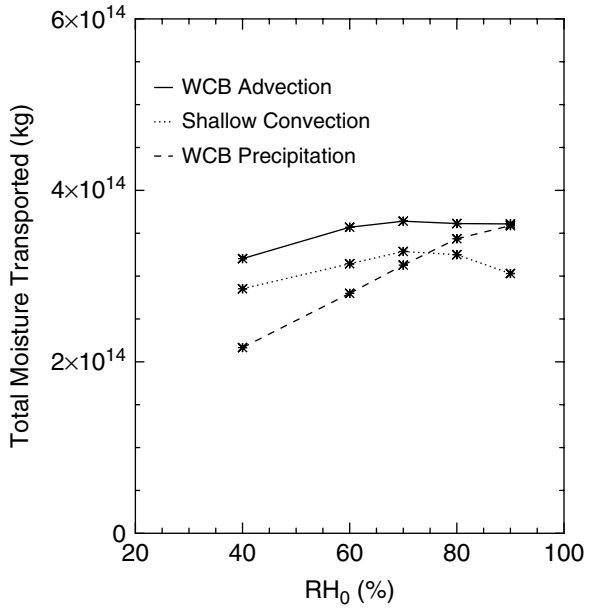

Figure 6. Total mass of moisture ventilated from the boundary layer (Q) by WCB advection (solid) and shallow convection (dotted) versus the initial value of RH_0. Also shown is the total WCB precipitation delivered by the life cycle (dashed).

(denoted $Q_{\rm conv}$) will be focused on. As discussed in section 3, $Q_{\rm wcb}$ is measured by resolved quantities and integrated over the WCB area, whilst for $Q_{\rm conv}$ we obtain the product $(\rho q)_h w_h$ from the convection scheme and integrate over points at which convection is occurring. It is possible that ventilation can occur by large-scale advection that is not in the WCB: however, direct computation demonstrates this residual term to be small. Therefore, Q represents the time integral of each process shown in Figure 3. $\mathcal{T} = 14$ days is chosen as a fixed time-scale to average over, and the way in which the cyclone lifetime might change with the variation of large-scale parameters will not be considered. In all simulations presented, the ventilation has peaked before day 14 and any ventilation after this time does not significantly affect the value of Q. The variation of w_h and q_h, i.e. the flux of moisture out of the boundary layer, is the primary focus here.

4.1. *Relative humidity*

The relative humidity profile chosen for the control simulation was representative of the wintertime storm track climatology, based on a comparison with reanalysis data shown in Pavan *et al.* (1999). As shown in Eq. (2), the tropospheric RH profile is proportional to its maximum (surface) value, denoted RH_0. In the control simulation $RH_0 = 80\%$ is used, and this value will be varied here to identify the effects of RH changes on the cyclone moisture cycle. Figure 5 shows a time series of EKE for various values of RH_0. The difference in atmospheric moisture starts to affect the cyclone development at day 4, shown by the diverging EKE curves in the figure. However, there are modest differences between the experiments throughout the life cycle, with all curves growing at a similar rate and peaking at the same time before decaying. There is a slight trend that higher values of RH_0 lead to higher EKE. This is to be expected, since the increased moisture intensifies the system through latent-heat release (Emanuel *et al.*, 1987; Ahmadi-Givi *et al.*, 2004), but the variation is small.

The reasons for the similarity between experiments with different RH_0 values can be understood in terms of the moisture cycle discussed in section 3. Figure 6 shows how $Q_{\rm wcb}$ and $Q_{\rm conv}$ vary with RH_0. The figure shows that Q from either process is largely insensitive to changes in RH_0, demonstrating that boundary-layer ventilation, by both advective and convective processes, has only a weak dependence on the initial RH profile.

The reason for this is that, over a sea surface, moisture is freely available to be evaporated from the sea, and this supplies moisture that is ultimately ventilated. For the control simulation, Boutle *et al.* (2010) demonstrated that the boundary-layer moisture budget is balanced, with input from evaporation balanced by ventilation. Similarly, the reanalysis data shown in figure 2 of Pavan *et al.* (1999) demonstrates that the long-term average near-surface RH is around 80% in midlatitude regions. Therefore it seems appropriate to define $RH_{\rm eq} = 80\%$ as the equilibrium value of boundary-layer RH. When $RH_0 < RH_{\rm eq}$, evaporation from the sea surface increases to restore equilibrium. The time-scale to obtain equilibrium can be estimated as the ratio of the moisture required to the rate of moisture input, namely

$$\tau_{\rm adj} = \frac{\rho q_{\rm sat} h (RH_{\rm eq} - RH_0)}{\rho C_H |\mathbf{v}_1| q_{\rm sat} (1 - RH)}, \qquad (4)$$

where h is the boundary-layer depth, C_H is the Stanton number, $|\mathbf{v}_1|$ is the wind speed at the lowest model level and the subscript 'sat' denotes the value of a quantity at saturation. Equation (4) assumes that ventilation of moisture can be ignored, which Figure 3 shows to be reasonable in the first 4 days of the life cycle. We then estimate $h \approx 1$ km, $C_H \approx 2 \times 10^{-3}$ and $|\mathbf{v}_1| \approx 5\,\mathrm{m\,s^{-1}}$, and $RH = RH_{\rm eq}$ is taken as an upper bound for the actual boundary-layer relative humidity. These values give $\tau_{\rm adj} = 2.3$ days when $RH_0 = 40\%$, decreasing to zero as RH_0 is increased to 80%. Therefore, the adjustment time-scale of the boundary-layer moisture content is fast compared with the life-cycle time-scale, and so the boundary-layer moisture content is

close to its equilibrium value throughout the life cycle and therefore ventilation is not sensitive to RH_0. There is a slight reduction in Q for very low RH_0, due to the reduced amount of moisture available to be ventilated in early stages of the life cycle, i.e. when $t \leq \tau_{\text{adj}}$. In a similar manner, when $RH_0 > RH_{\text{eq}}$, the evaporation is reduced whilst ventilation is unchanged until RH_{eq} is reached within the boundary layer. An interesting aside is that this is only true for the slowly developing baroclinic waves being considered. Equation (4) demonstrates why the initial RH profile is important for 'bomb' cyclones, which develop over ≈ 1 day and have no time for RH to adjust to its equilibrium state.

Figure 6 also shows the total mass of moisture returned to the surface by WCB precipitation, which does vary with RH_0. For the control value, $RH_0 = 80\%$, the total precipitation is approximately equal to the total moisture ventilated on the WCB, as discussed in section 3. However, for lower values of RH_0 the total precipitation delivered is lower, demonstrating that the WCB is no longer 100% efficient at converting moisture ventilated into precipitation. Instead, some of the moisture ventilated is retained within the atmosphere, modifying the background RH profile in the free troposphere.

This finding can explain the time series shown in Figure 5. For different values of RH_0, the large-scale cyclone dynamics initially follows the same evolution. The surface evaporation, boundary-layer transport and ventilation are similar in all experiments. However, precipitation formation is weakened at lower values of RH_0, since the free troposphere, where most of the precipitation forms, is further from saturation and needs to be moistened before precipitating cloud can form. Therefore, the precipitation rate is initially lower, demonstrating why the curves diverge at such an early time due to the modified latent-heat release. Moisture accumulates within the atmosphere, modifying the RH profile, which then approaches that of the control experiment. Later in the life cycle the RH profiles are very similar, forcing similar cyclone development towards the end of the life cycle. For increased initial moisture content ($RH_0 = 90\%$) there is intense precipitation from an early stage of the life cycle. This releases large amounts of latent heating in the mid-troposphere, which forces a more intense cyclone system to develop. As shown in Figure 5, however, the EKE returns to values typical of lower RH_0 later in the life cycle (around day 10) when the precipitation rate is reduced.

These simulations show why, for midlatitude regions, the RH profile remains approximately constant. If, for any reason, the RH profile is moved away from its equilibrium state, evaporation and precipitation processes driven by the large-scale cyclone dynamics redistribute moisture until the equilibrium state is returned. This adjustment process is fast and can happen within one cyclone life cycle. Figure 7 shows the zonal-mean relative humidity from simulations at day 14 with $RH_0 = 80\%$ and 0% respectively. It can be seen that between 30–60°N and up to 200 hPa (the region this cyclone system influences) the two simulations are similar qualitatively and even quantitatively, demonstrating that even a single life cycle can create a profile close to climatology. The cyclone has not produced any moisture transport further north than 60°N, although this is a feature of our initial conditions and differences in storm track orientation could lead to cyclones transporting moisture further north. The system has also not exported any moisture into the stratosphere, meaning other processes are important for this transport.

4.2. *Absolute temperature*

Dry simulations of cyclogenesis are not affected by the absolute temperature of the atmosphere – only the meridional temperature gradient is important (see, for example, the Eady (1949) model). Section 4.1 demonstrated that the initial moisture content of the atmosphere does not affect the cyclone moisture cycle to any great extent, since the atmosphere quickly recovers its equilibrium relative humidity by evaporation and precipitation processes. The absolute temperature of the atmosphere determines the saturation vapour pressure, and so should affect the moisture cycle and hence possibly the large-scale development of the system via higher latent-heat release.

We investigate these possibilities through a series of simulations in which a constant value is added to or subtracted from the atmospheric and surface-temperature profiles. The temperature changes will be interpreted in terms of the surface temperature at 45°N (the jet centre). For the control simulation, $T_0 = 280$ K. The relative humidity profile is fixed across all experiments and therefore the specific humidity profile changes for each simulation, dependent on the atmospheric temperature. Figure 8 shows the evolution of EKE for several simulations with different temperatures. The general trend is that a higher temperature leads to more intense systems.

Figure 9 shows the variation of Q with T_0. As anticipated by the Clausius–Clapeyron equation, there is a strong relation between the moisture ventilated and the absolute temperature. These results are consistent with those presented by Allen and Ingram (2002) and Field and Wood (2007). Field and Wood (2007) demonstrated that an increase of 7 K in the SST led to an approximately 50% increase in precipitation rate, whilst Allen and Ingram (2002) suggested that if precipitation increased at the same rate as the global increase in atmospheric water-vapour storage then there should be a $6.5\%\,\text{K}^{-1}$ increase. Both of these quantitative predictions fit well with the observed variation in these simulations. The variation in WCB precipitation closely matches what would be expected from the Clausius–Clapeyron relation, as shown in Figure 9, whilst the WCB advection and shallow convection have a slightly stronger variation, especially at higher temperatures. This is likely to be due to a positive feedback within the system – at very high temperatures, there is so much latent heat release that w_h is increased. Examination of the model output has shown that w_h does show a slight increase as T_0 is increased. Therefore, most of the variation in Q can be explained by the change in q_h due to Clausius–Clapeyron, and the additional variation comes from the higher values of w_h. The precipitation efficiency of the WCB drops slightly at higher temperatures since, although the initial RH is fixed across all simulations, the troposphere is not saturated and can be moistened by the WCB. At higher temperatures, the increased saturation vapour pressure means a greater quantity of moisture can remain in the troposphere.

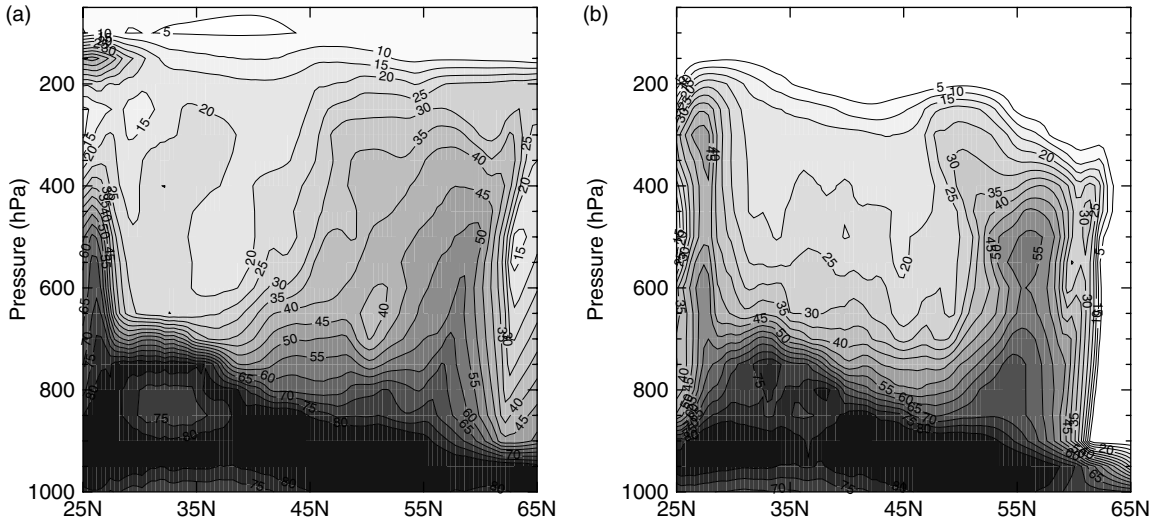

Figure 7. Zonal-mean relative humidity (contoured, interval 5%) at day 14 from (a) the control simulation, i.e. $RH_0 = 80\%$, and (b) a simulation in which $RH_0 = 0\%$.

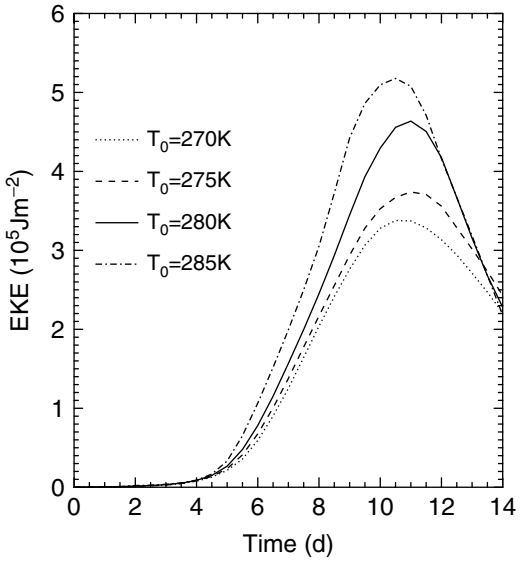

Figure 8. Time series of eddy kinetic energy for various values of the initial surface temperature at 45°N (shown on the plot).

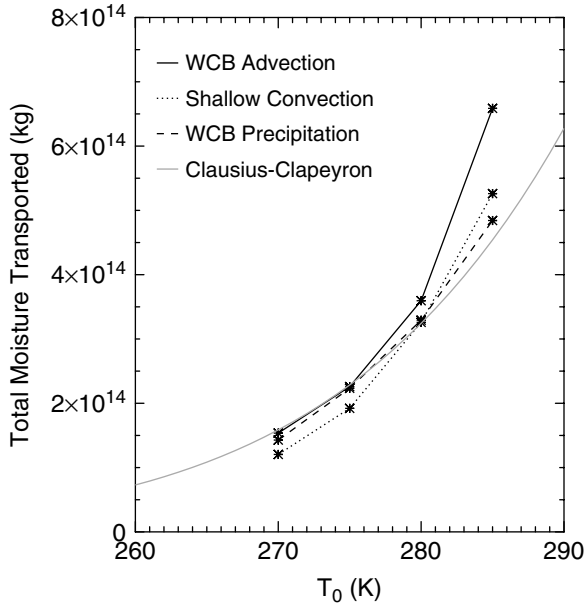

Figure 9. Total mass of moisture ventilated from the boundary layer (Q) by WCB advection (solid) and shallow convection (dotted) versus the initial value of T_0. Also shown is the total WCB precipitation delivered by the life cycle (dashed) and the Clausius–Clapeyron relation (grey).

4.3. *Meridional temperature gradient*

The meridional temperature gradient, characterized by the peak jet speed (U_0), is known to be one of the three key large-scale parameters affecting cyclone evolution. The others, as shown by the Eady (1949) model, are the static stability (N) and Coriolis parameter (f). A recent article by Sinclair *et al.* (2010) has discussed how these three parameters affect boundary-layer ventilation of a passive tracer in dry baroclinic-wave life cycles (identical to our control simulation but with no moisture present). In this section, we focus on the meridional temperature gradient as a large-scale driver of cyclone intensity. The meridional temperature gradient is the most variable of these three parameters, changing on seasonal time-scales (the winter jet is stronger than the summer jet), interannual time-scales (the NAO exerts control on the jet strength) and climatological time-scales (the meridional temperature gradient may change as the climate changes).

The peak jet speed was defined to be $U_0 = 45\,\mathrm{m\,s^{-1}}$ in the control simulation (Eq. (1)). Figure 10 shows the time series of EKE for simulations with various values of U_0. As anticipated, the jet strength acts as a sensitive control on the cyclone intensity, with faster jet speeds forcing stronger cyclone systems.

The variation of Q with U_0 is shown in Figure 11, and reveals a strong dependence. A regression on a log plot shows the dependence to be $Q \sim U_0^3$. The results presented by Sinclair *et al.* (2010) demonstrated that $w_h \sim U_0^2$ and it is anticipated that, for the large-scale ascent, this relationship should hold true here. There must therefore be an additional scaling of $q_h \sim U_0$, which can be explained in terms of the moisture cycle as follows. According to thermal wind balance, if U_0 changes then so does the meridional temperature gradient. T_0 is held constant across this set

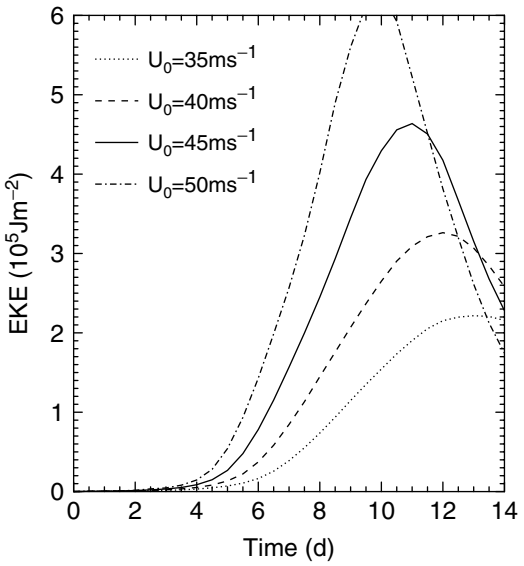

Figure 10. Time series of eddy kinetic energy for various values of the peak jet speed (shown on the plot).

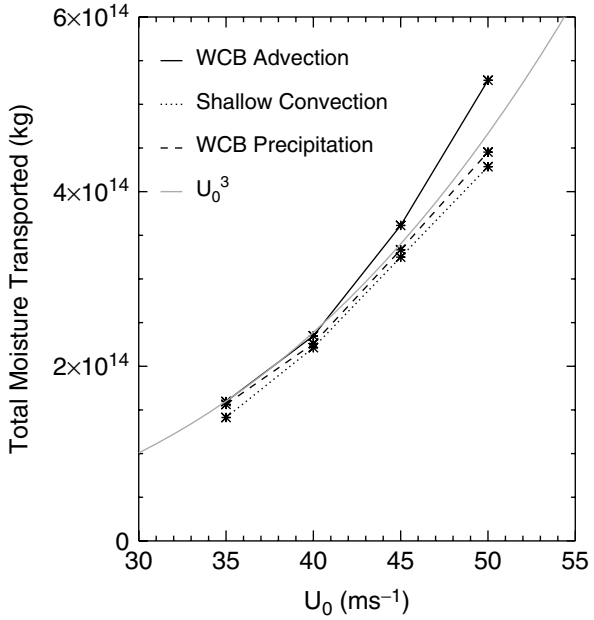

Figure 11. Total mass of moisture ventilated from the boundary layer (Q) by WCB advection (solid) and shallow convection (dotted) versus the initial value of U_0. Also shown is the total WCB precipitation delivered by the life cycle (dashed) and a U_0^3 scaling (grey).

of simulations and so for increased U_0, the air (and SST) to the south of the jet is higher. This increases the potential for the atmosphere in this region to retain more moisture, as demonstrated in section 4.2. Boutle *et al.* (2010) demonstrated that the moisture ventilated has its origin to the south of the jet centre, within the high-pressure part of the wave. Therefore it appears that q_h has been increased by the higher temperatures in the source of the moisture. The reasons for the linear scaling will be discussed next.

It is worth noting that real-world variation in U_0 is often achieved by a greater temperature change on the polar side of the jet, with only small variations in the temperature on the tropical side. Therefore, in our framework, a change to U_0 would be accompanied by a change to T_0 and the sense of the T_0 change would act to offset some of the variation of q_h with U_0.

5. Scaling moisture ventilation

Scaling arguments can be used to assess quantitatively how changes in one or more variables will affect cyclone characteristics and, in this case, moisture ventilation. Each of the factors in Eq. (3) will need to be scaled to establish the dependence of the total moisture ventilated over a life cycle. As stated previously, $\mathcal{T} = 14$ days will be used for the time-scale of a cyclone life cycle, and thus the scalings developed will be equally applicable to the total moisture ventilated or the average flux of moisture out of the boundary layer.

5.1. *Scaling ventilation by the warm conveyor belt*

Sinclair *et al.* (2010) developed a scaling for w_h based on the theory of baroclinic instability. Either by applying scaling arguments to the relevant terms in the QG omega equation or from the Eady model they obtained

$$w_h \sim \frac{v_g f \dfrac{\partial u_g}{\partial z}}{2N^2}, \tag{5}$$

where u_g and v_g are the geostrophic zonal and meridional wind speeds. They also demonstrated that $v_g \sim U_0$ and $\partial u_g/\partial z \sim U_0/z_T$. Therefore, they obtained a scaling for w_h in terms of parameters of the initial condition and demonstrated that the WCB ascent in the dry version of our control experiment closely matched Eq. (5). In our control simulation the ascent rate is enhanced on the WCB, but the scaling argument still applies. It is found that $v_g = 0.36U_0$ gives a very close numerical match between the observed WCB ascent rate and the prediction of Eq. (5).

Sinclair *et al.* (2010) also scaled the area of the WCB as follows:

$$\mathcal{A} = \left(\frac{\pi a}{2m}\right)^2, \tag{6}$$

where a is the radius of the Earth and $m = 6$ is the zonal wavenumber of the simulations. This was based on the assumption that the WCB area was approximately a quarter of the total wavelength. Comparison with model output from the control simulation (not shown) demonstrates that this approximation is too large by a factor of two, and so $\mathcal{A}_{\mathrm{wcb}} = \mathcal{A}/2$ is used for the scalings presented here.

In these simulations, the density $\rho_h \approx 1\,\mathrm{kg\,m^{-3}}$ and is approximately constant. Finally we require a scaling for q_h. Providing that the partial pressure of water vapour in air is small compared with the atmospheric pressure,

$$q \approx \frac{RHe_{\mathrm{sat}}}{1.61p}, \tag{7}$$

where p is the atmospheric pressure and e_{sat} is the saturation vapour pressure. Quantity e_{sat} is a function of temperature, governed by the Clausius–Clapeyron equation, for which an empirical approximation (Bolton, 1980) is used here, which when substituted into Eq. (7) gives

$$\begin{aligned} q &\approx \frac{RH}{1.61p} 6.112 \exp\left[\frac{17.67(T-273.15)}{T-29.65}\right] \\ &= \frac{RH}{1.61p}\mathcal{C}(T), \end{aligned} \tag{8}$$

where $\mathcal{C}(T)$ is introduced to represent the empirical solution to the Clausius–Clapeyron equation as a function of temperature (T). To obtain a representative value of q_h, it is therefore necessary to obtain scalings for T_h, RH_h and p_h, i.e. boundary-layer top values are required since this is where the ventilation is occurring. Comparison with model output demonstrates that the boundary layer is well mixed in relative humidity, and therefore $RH_h \approx RH_{\rm eq} = 80\%$. $p_h \approx 900$ hPa is used as a typical value of pressure near the boundary-layer top. As discussed in section 4.3, most of the moisture ventilated has its origins to the south of the jet, and therefore a temperature appropriate for the southern part of the domain is required. The jet is prescribed analytically and the temperature profile obtained from thermal wind balance, so a scaling for T_h based on thermal wind balance is adopted here:

$$\frac{g}{T_{45^\circ\rm N}}\frac{\partial T}{\partial y} = -f\frac{\partial u}{\partial z} \Rightarrow \frac{g}{T_{45^\circ\rm N}}\frac{T_{45^\circ\rm N} - T_h}{\mathcal{L}} \sim -f\frac{U_0}{z_T}, \quad (9)$$

where g is the gravitational acceleration and $T_{45^\circ\rm N}$ is a typical value of the boundary-layer top temperature at 45°N. $\mathcal{L} = \sqrt{\mathcal{A}}$ is a horizontal length-scale, which does not vary between experiments due to the fixed wavenumber used in this study. Rearranging Eq. (9) gives

$$T_h \sim T_{45^\circ\rm N}\left(1 + \frac{fU_0\mathcal{L}}{z_T g}\right). \quad (10)$$

In practice, $T_{45^\circ\rm N} = T_0$ is too high to be representative of the boundary-layer top temperature, and therefore $T_{45^\circ\rm N} = T_0 - 5$ is used. 5 K is typical of the drop in temperature across the boundary layer and this value gives a close match between q_h defined by Eq. (8) and the observed values of q_h within the model.

Combining these scaling arguments gives the following formula for moisture ventilation by the WCB:

$$\begin{aligned} Q_{\rm wcb} &= \rho_h \mathcal{T}\frac{1}{2}\left(\frac{\pi a}{2m}\right)^2 \frac{0.36fU_0^2}{2N^2 z_T} \\ &\quad \times \frac{RH_{\rm eq}}{1.61p_h}\mathcal{C}\left[(T_0 - 5)\left(1 + \frac{fU_0\mathcal{L}}{z_T g}\right)\right]. \quad (11) \end{aligned}$$

5.2. *Scaling ventilation by shallow convection*

A scaling for the convective ventilation is also desired, to establish why the convection appears to scale in the same manner as the large-scale ventilation in sections 4.1-4.3. $\mathcal{T}$ is identical for the convective ventilation, whilst model output (not shown) demonstrates that $\mathcal{A}_{\rm conv} \approx \mathcal{A}$, where $\mathcal{A}_{\rm conv}$ is defined as the number of grid points that contribute to the convective ventilation. The convection occupies approximately a quarter of a wavelength, behind the low centre. As discussed in Boutle *et al.* (2010), the convection forms behind the cold front, in a cold-air outbreak. It is driven by the large-scale dynamics of the cyclone system, which create the positive surface fluxes of sensible and latent heat that drive the convection. To estimate the moisture flux, consider a steady-state boundary layer in which the convective ventilation is entirely governed by the surface-moisture flux, namely

$$\overline{w'q'}_{\rm conv} \sim \overline{w'q'}_0 = C_H|\mathbf{v}_1|(q_{\rm sat}(\theta_s) - q_1), \quad (12)$$

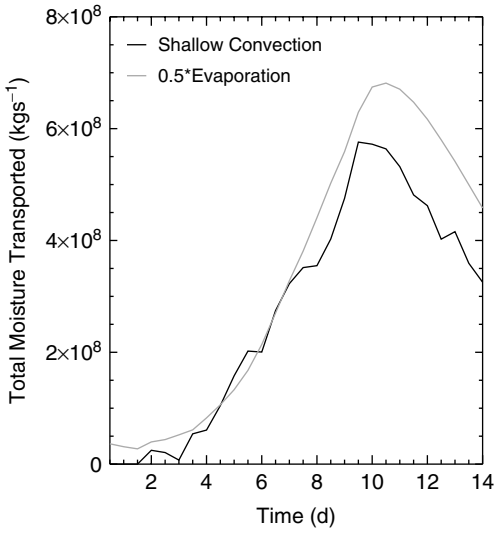

Figure 12. Time series of total moisture ventilated by shallow convection (black) and half the total moisture input from evaporation (grey), for the control simulation.

where $\overline{w'q'}$ is the turbulent moisture flux and θ_s is the surface temperature. It is found that the convective ventilation is approximately half of the surface-moisture flux at any time, i.e. $\overline{w'q'}_{\rm conv} \approx 0.5\overline{w'q'}_0$. This is shown in Figure 12 for the control simulation, although a similar relation can be found for any of the other experiments conducted. Although C_H is a complex function of the Obukhov length, for simplicity it is assumed constant and of value 2×10^{-3}, which is representative of the convective boundary-layer region over which the convection occurs. $|\mathbf{v}_1|$ is governed by the large-scale cyclone parameters, driven by the large-scale ascent on the WCB forcing convergence of near-surface winds into frontal regions. Therefore, it is scaled by the continuity equation as follows:

$$\frac{\partial u}{\partial x} + \frac{\partial v}{\partial y} = -\frac{\partial w}{\partial z} \Rightarrow |\mathbf{v}_1| \sim \frac{w_h}{h}\mathcal{L}. \quad (13)$$

Finally, $q_{\rm sat}$ and q_1 are given by Eq. (8) as a function of T, p and RH. T is estimated using Eq. (10) to be representative of the location of the convecting region, which is to the south of the jet. Here, surface values are required and therefore $RH = RH_{\rm eq} = 80\%$ is used for q_1 and $RH = RH_{\rm sat} = 100\%$ is used for $q_{\rm sat}$. $p = p_0 = 1000$ hPa and $T_{45^\circ\rm N} = T_0$ are used as representative values near the surface, whilst $h \approx 1$ km is used as a typical value of the boundary-layer depth.

Combining these scaling arguments gives the moisture ventilation by shallow convection as

$$\begin{aligned} Q_{\rm conv} &= \rho_h \mathcal{T}\left(\frac{\pi a}{2m}\right)^2 \frac{1}{2}C_H\frac{\mathcal{L}}{h}\frac{0.36fU_0^2}{2N^2 z_T} \\ &\quad \times \frac{RH_{\rm sat} - RH_{\rm eq}}{1.61p_0}\mathcal{C}\left[T_0\left(1 + \frac{fU_0\mathcal{L}}{z_T g}\right)\right]. \quad (14) \end{aligned}$$

5.3. *Comparison of scalings with simulations*

The scalings presented in Eqs (11) and (14) show how the moisture ventilated varies with T_0 and U_0. For the large changes in T_0 discussed in section 4.2, the Clausius–Clapeyron relation $\mathcal{C}(T)$ produces strong nonlinear changes to Q. However, the changes to U_0

discussed in section 4.3 produce only small changes to T, and the Clausius–Clapeyron relation is in a region of almost linear variation. This explains the apparent U_0^3 variation of Q observed in section 4.3: the correct scaling should be $Q \sim U_0^2 \mathcal{C}(T)$. However, for the values of U_0 used, $\mathcal{C}(T) \sim U_0$. Equations (11) and (14) also suggest some additional factors that may influence Q; for example, there should be an f^2 and N^{-2} dependence of the ventilation. Therefore, four further experiments were performed. Two of these varied the initial values of tropospheric stability from the control value of 4 K km^{-1} to a more stable value of 6 K km^{-1} and a less stable value of 3.5 K km^{-1}. The other two varied the jet latitude from the control value of 45°N to 40°N and 50°N respectively, thus varying the Coriolis parameter. For these experiments, the use of Cartesian geometry is important, since it ensures that only f changes, with $\mathcal{A}$ remaining constant.

Figure 13 shows the expected values of Q obtained from Eqs (11) and (14) plotted against the observed values from the full range of simulations conducted. A strong correlation is shown for both the advective and convective scaling arguments, with correlation coefficients in excess of 0.97. The points are also scattered closely around the 1 : 1 line, demonstrating that the magnitude and variation of ventilation given by the scaling arguments is reasonable. Both plots do however show a gradient slightly less than 1, found to be ≈ 0.7 in both cases. This seems likely to be due to latent-heat release feeding back into cyclone development. In both scaling arguments, the cyclone intensity, characterized by w_h (Eq. (5)), and the moisture content, characterized by q_h (Eq. (8)), have been assumed to be independent. However, as discussed in sections 4.1 and 4.2, they are not independent, since increased moisture leads to a more intense cyclone, as shown in Figures 5 and 8.

6. Surface-moisture availability

The warm conveyor belt is a large-scale, cyclone-driven process and so it is expected to be largely insensitive to changes in the boundary-layer structure. For example, Sinclair *et al.* (2010) demonstrated that tracer ventilation on the WCB was insensitive to the amount of boundary-layer drag applied. However, shallow convection is very closely linked to the boundary-layer structure beneath the cloud base, and so it is anticipated that convective moisture ventilation will be affected differently from WCB ventilation.

To investigate how the two ventilation processes vary differently with possible changes to the boundary-layer structure, the surface-moisture availability has been chosen as the parameter to change. All experiments discussed so far have been conducted over a sea surface, and therefore moisture is freely available to be evaporated from the sea. However, cyclones regularly track over land (for example at the end of the North Atlantic and Pacific storm tracks) and can also form over land (for example over the central USA in the lee of the Rocky Mountains). Instead of implementing a full land-surface scheme with surface-energy balance, a simplified view is taken here, consistent with the idealized modelling strategy. Within the model, the surface-moisture flux is adjusted thus:

$$E_s = \alpha \rho C_H |\mathbf{v}_1| (q_{\mathrm{sat}}(\theta_s) - q_1), \tag{15}$$

where $\alpha \in [0, 1]$ is a parameter describing the surface-moisture availability. $\alpha = 1$ results in the control simulation, whilst $\alpha = 0$ would result in no surface evaporation, with values in between representing various levels of moisture availability.

A series of experiments was conducted with various values of α. Results are shown in Figure 14. As expected, the changes to the surface evaporation do not have a great affect on the large-scale development of the system. There is a general trend of higher EKE for experiments with higher values of α, caused by the increased moisture leading to greater latent-heat release and so more intense systems.

Figure 15 shows the moisture ventilation plotted against α for this series of experiments. It is immediately clear that modifying the surface-moisture availability has affected the moisture transport in distinctly different ways. Both the advective and convective ventilation appear to vary linearly with α, but with a different gradient. The large-scale transport reduces from its peak value of $\approx 3.6 \times 10^{14}$ kg to a value of $\approx 1.9 \times 10^{14}$ kg as α is reduced towards zero. It appears that if there were no evaporation the amount of ventilation would be approximately half the value when $\alpha = 1$. This is because, even when there is no evaporation, there is some atmospheric moisture in the initial condition which is ventilated on the WCB. However, once this moisture has been ventilated (and eventually precipitated from the atmosphere), there is no evaporation to replace the lost moisture. Therefore, the ventilation rate drops off quickly towards the end of the life cycle, since q_h is reduced.

The convective ventilation reacts differently however, since, as discussed in section 5.2, the triggering of convection is closely linked to the surface fluxes of heat and moisture. When the surface-moisture flux is zero, a single mixed layer grows above the surface and moist convection is never triggered. Therefore, there is no convective ventilation. Figure 16 shows a tephigram at the same time and location from two experiments with $\alpha = 1$ and $\alpha = 0.2$. When $\alpha = 0.2$, there is a single mixed layer with constant potential temperature and specific humidity extending up to ≈ 850 hPa. There is then a strong inversion in the potential temperature profile above this, with no convective available potential energy (CAPE), and therefore no convection can occur. When $\alpha = 1$, the near-surface potential temperature is unchanged but the increased evaporation has increased the moisture content of the boundary layer from ≈ 5 g kg^{-1} to ≈ 7 g kg^{-1}. A Normand's construction now shows a lifting condensation level at ≈ 900 hPa, with an area of CAPE extending up to an inversion at ≈ 750 hPa. There is therefore a well-mixed boundary layer below 900 hPa, with an area of cumulus convection above this, producing a large amount of convective ventilation.

Figure 15 also shows how the ventilation is expected to vary from the scaling arguments presented in section 5, with some minor modifications. As demonstrated in section 4.1, when $\alpha = 1$ and moisture is freely available from the surface, the boundary-layer RH (or equivalently q_h) remained approximately constant throughout the life cycle. However, as α is decreased and moisture availability is restricted, the boundary-layer RH reduces as the life cycle evolves. When $\alpha = 0$ and there is no convective ventilation, we can estimate the time-scale over which we expect the boundary-layer moisture content to reduce to zero. This is given by the ratio of the initial moisture content to the removal rate

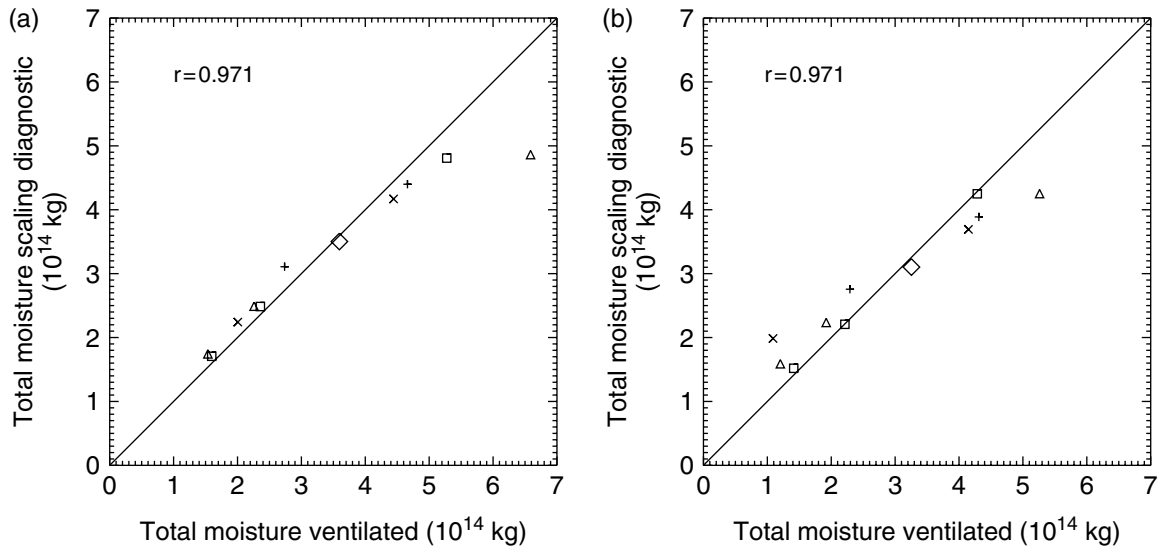

Figure 13. Scatter plots showing the observed values of Q from direct model output versus the scaled diagnostic of moisture ventilation for (a) the advective WCB ventilation and (b) the convective ventilation. The diamond represents the control run, with other simulations performed with varied values of T_0 (triangles), U_0 (squares), N^2 (crosses) and f (plus signs). The Pearson correlation coefficient is also shown.

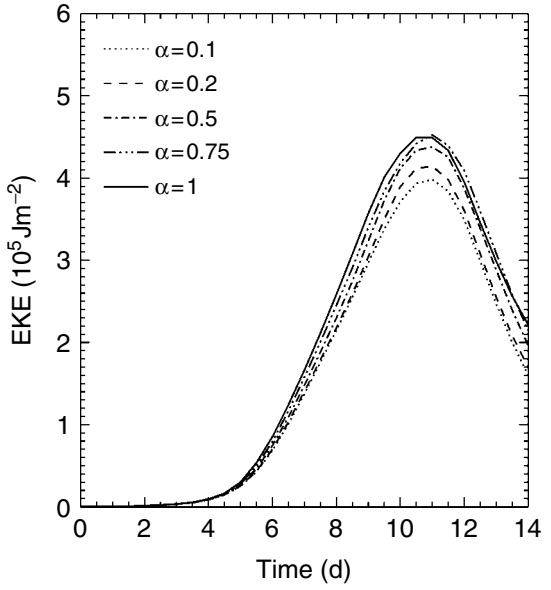

Figure 14. Time series of eddy kinetic energy for various values of α (shown on the plot).

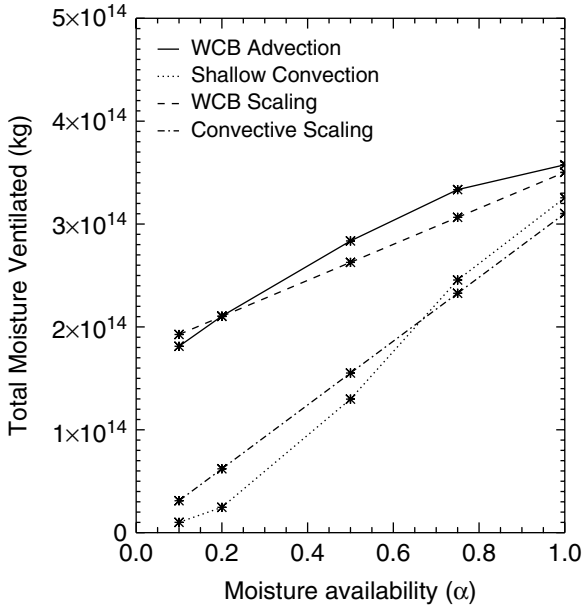

Figure 15. Total mass of moisture ventilated from the boundary layer (Q) by WCB advection (solid) and shallow convection (dotted) versus α. Also shown are the results of the scaling arguments discussed in the text, for large-scale advection (dashed) and shallow convection (dot–dashed).

on the WCB, i.e.

$$\tau_{\rm rem} = \frac{\rho q_{\rm BL} h \mathcal{A}_{\rm cyc}}{\rho q_h w_h \mathcal{A}_{\rm wcb}}. \tag{16}$$

Again, we estimate $h \approx 1$ km and use the scalings of Eq. (5) for w_h and Eq. (6) for $\mathcal{A}_{\rm wcb}$. $\mathcal{A}_{\rm cyc}$ is the total area of boundary layer that can be ventilated by the cyclone, which is given by $8\mathcal{A}$. This is because the cyclone can ventilate an entire wavelength in the zonal direction ($4\mathcal{L}$) and approximately 30° ($2\mathcal{L}$) in the meridional direction. A lower bound of $\tau_{\rm rem} \approx 9.5$ days is found when $q_{\rm BL} = q_h$, which is a reasonable assumption to make because divergent and convergent motions within the boundary layer ensure that the WCB footprint always contains any available moisture for ventilation. This value is a lower bound because subsidence and entrainment of moisture from the troposphere into the boundary layer has been neglected, although Boutle *et al.* (2010) demonstrated these terms in the boundary-layer moisture budget to be small compared with the WCB ascent. Therefore, it appears reasonable that over the life cycle the WCB can ventilate all moisture initially contained within the boundary layer.

The scalings presented in section 5 require a constant value of all variables throughout the life cycle, and so an average value of 40% for the boundary-layer RH when $\alpha = 0$ seems appropriate for use in Eq. (11). When $\alpha = 1$, section 5 has demonstrated that $RH = RH_{\rm eq} = 80\%$, and so a simple linear variation of the average value of RH with α gives

$$RH = RH_{\rm eq}\frac{1+\alpha}{2}, \tag{17}$$

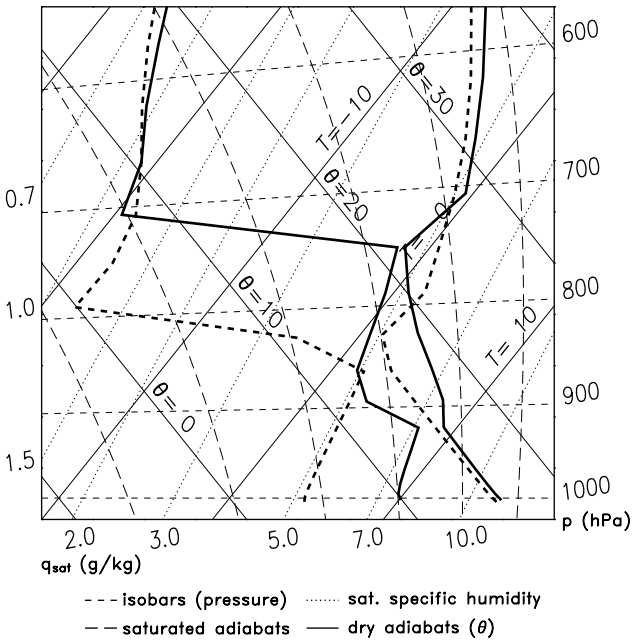

Figure 16. Tephigram in the shallow convective region (−27.6°E, 36.8°N) at day 7, showing experiments with $\alpha = 1$ (solid) and $\alpha = 0.2$ (dashed).

which is used in Eq. (11) and gives good agreement with the measured values of Q_{wcb} in Figure 15.

Section 5.2 discussed how the convective ventilation is proportional to the surface-moisture flux, and therefore the scaling for convective ventilation, given in Eq. (12), is modified thus:

$$\overline{w'q'}_{\mathrm{conv}} \sim \alpha C_H |\mathbf{v}_1| (q_{\mathrm{sat}}(\theta_s) - q_1). \tag{18}$$

This introduces a factor of α into Eq. (14), and Figure 15 also shows this scaling to be in good agreement with the observed values of Q_{conv}.

7. Conclusions

This article has shown from a combination of numerical experiments and simple scaling arguments how boundary-layer moisture ventilation varies with changes to large-scale and boundary-layer parameters. Whilst results and scaling arguments have typically been presented in terms of the moisture ventilated from the boundary layer, it is important to note that moisture transport can be thought of as a proxy for many other processes. Boutle *et al.* (2010) demonstrated how the large-scale ventilation on the WCB was balanced by a convergence of moisture within the boundary layer, which is, in turn, balanced by divergence of moisture from anticyclonic regions of the baroclinic wave. It was also discussed how the WCB is close to 100% efficient at converting ascending moisture into precipitation (Eckhardt *et al.*, 2004), and therefore the scalings presented for WCB ventilation also describe how the WCB precipitation is likely to vary.

A strong dependence of the moisture transport on the jet strength has been demonstrated, with $Q \sim U_0^3$. This is in good agreement with the results of Stohl *et al.* (2008), who demonstrate a strong dependence of poleward moisture transport and precipitation on the NAO. A positive NAO causes increased jet strength, and so the U_0^3 scaling shows why there is such a strong variation with the NAO. Ruprecht *et al.* (2002) also demonstrated increased moisture transport in positive NAO conditions due to the poleward shift in the jet, which has also been demonstrated from scaling arguments, with $Q \sim f^2$. It is worth noting that in both of these circumstances there is likely to be some offsetting to the moisture transport from a reduction in T_0, and that the orientation of the jet may change with the NAO, an effect that has not been considered here.

Field and Wood (2007) argued for a scaling of the WCB rain rate as follows:

$$R_{\mathrm{wcb}} = c\langle V \rangle \langle WVP \rangle, \tag{19}$$

where c depends on the cyclone area, the size of the WCB inflow and the asymmetry in moisture distribution within the cyclone. The scaling arguments presented here have demonstrated consistency with this scaling. It has been shown here that

$$R_{\mathrm{wcb}} = \widetilde{c} w_h q_h, \tag{20}$$

where continuity implies $\langle V \rangle \sim w_h$, whilst $\langle WVP \rangle \sim q_h$ since most moisture is contained within the boundary layer and so the effect of free-tropospheric moisture, included in $\langle WVP \rangle$, is small. $\widetilde{c}$ incorporates these proportionality relations and c. It has been shown here why q_h varies according to the Clausius–Clapeyron equation, a fact noted in Field and Wood (2007).

The scaling arguments also provide an interesting framework for interpreting climate model results. For example, it is anticipated that polar regions will warm faster than equatorial regions (Meehl *et al.*, 2007), there will be a poleward shift in the storm track (Yin, 2005) and an increase in midlatitude static stability (Frierson, 2006). The response of cyclone moisture transport and precipitation is therefore a complicated combination of these changes. The scalings suggests that increased global mean temperature will increase the moisture transport, but this could be offset by a reduction in the meridional temperature gradient (due to the polar regions warming faster). The poleward shift in the storm tracks should provide another mechanism for increased moisture transport, but this could again be offset by an increase in static stability. Therefore, even the sign of the midlatitude moisture transport and precipitation response is a complex combination of the magnitude of changes to several other variables, and whilst it seems likely that there will be an overall increase in midlatitude moisture transport (Held and Soden, 2006), the precise mechanism for this is unclear. Recent trends suggest that the frequency of cyclones is reducing (Paciorek *et al.*, 2002). Therefore, each system will require a larger increase in moisture transport (and precipitation) than the midlatitude mean to account for the reduced number of storms.

The scaling arguments have demonstrated the key physical variables that influence cyclone moisture transport and precipitation, but they also have many other potential uses. Their simplicity means that they can be used for climatological studies of moisture transport and precipitation and also for pollution ventilation with some minor modification. Sinclair *et al.* (2010) discussed how the large-scale advection could be used to create pollution-ventilation climatologies. The present work provides a similar scaling for ventilation by moist convection, a process that has been previously shown to be an efficient method

of pollution ventilation in the absence of frontal systems (Dacre *et al.*, 2007).

Section 6 has also demonstrated that although advective and convective processes are similarly constrained by the large-scale flow, they react very differently to boundary-layer changes. Sinclair *et al.* (2010) demonstrated that the WCB was controlled entirely by the large scale, and reasonable changes to the surface roughness had no effect on its ability to ventilate the boundary layer. This work has demonstrated a much closer link between convective ventilation and the boundary-layer structure, shown here in terms of moisture availability, but future work could investigate the dependence on the surface sensible heat and momentum fluxes. These results, combined with the results of Boutle *et al.* (2010), demonstrate the importance of boundary-layer processes to the midlatitude water cycle. Convectively ventilated moisture can be transported large distances in the troposphere and even become dynamically important near the cold front, but its evolution depends heavily on the surface-energy balance.

Acknowledgements

We thank Andy Brown of the Met Office, UK, and Bob Beare of the University of Exeter, UK, for helpful discussions of the work. I. Boutle is supported by NERC CASE award NER/S/C/2006/14273.

References

Ahmadi-Givi F, Craig GC, Plant RS. 2004. The dynamics of a midlatitude cyclone with very strong latent-heat release. *Q. J. R. Meteorol. Soc.* **130**: 295–323.

Allen M, Ingram W. 2002. Constraints on future changes in climate and the hydrologic cycle. *Nature* **419**: 224–232.

Balasubramanian G, Garner ST. 1997. The role of momentum fluxes in shaping the life cycle of a baroclinic wave. *J. Atmos. Sci.* **54**: 510–533.

Bengtsson L, Hodges KI, Roeckner E. 2006. Storm tracks and climate change. *J. Climate* **19**: 3518–3543.

Bolton D. 1980. The computation of equivalent potential temperature. *Mon. Weather Rev.* **108**: 1046–1053.

Boutle IA, Beare RJ, Belcher SE, Brown AR, Plant RS. 2010. The moist boundary layer under a midlatitude weather system. *Boundary-Layer Meteorol.* **134**: 367–386.

Dacre HF, Gray SL, Belcher SE. 2007. A case study of boundary layer ventilation by convection and coastal processes. *J. Geophys. Res.* **112**: D17106.

Eady ET. 1949. Long waves and cyclone waves. *Tellus* **1**: 33–52.

Eckhardt S, Stohl A, Wernli H, James P, Forster C, Spichtinger N. 2004. A 15-year climatology of warm conveyor belts. *J. Climate* **17**: 218–237.

Emanuel K, Fantini M, Thorpe A. 1987. Baroclinic instability in an environment of small stability to slantwise moist convection. Part I: Two-dimensional models. *J. Atmos. Sci.* **44**: 1559–1573.

Field PR, Wood R. 2007. Precipitation and cloud structure in midlatitude cyclones. *J. Climate* **20**: 233–254.

Field PR, Gettelman A, Neale RB, Wood R, Rasch PJ, Morrison H. 2008. Midlatitude cyclone compositing to constrain climate model behaviour using satellite observations. *J. Climate* **21**: 5887–5903.

Frierson DMW. 2006. Robust increases in midlatitude static stability in simulations of global warming. *Geophys. Res. Lett.* **33**: L24816.

Gutowski WJ, Jiang W. 1998. Surface-flux regulation of the coupling between cumulus convection and baroclinic waves. *J. Atmos. Sci.* **55**: 940–953.

Held IM, Soden BJ. 2006. Robust responses of the hydrological cycle to global warming. *J. Climate* **19**: 5686–5699.

Martin GM, Ringer MA, Pope V, Jones A, Dearden C, Hinton T. 2006. The physical properties of the atmosphere in the new Hadley Centre Global Environment Model (HadGEM1). Part I: Model description and global climatology. *J. Climate* **19**: 1274–1301.

Meehl GA, Stocker TF, Collins WD, Friedlingstein P, Gaye AT, Gregory JM, Kitoh A, Knutti R, Murphy JM, Noda A, Raper SCB, Watterson IG, Weaver AJ, Zhao ZC. 2007. 'Global climate projections'. In *Climate Change 2007: The Physical Science Basis*. Cambridge University Press: Cambridge, UK.

Paciorek CJ, Risbey JS, Ventura V, Rosen RD. 2002. Multiple indices of Northern Hemisphere cyclone activity, winters 1949–99. *J. Climate* **15**: 1573–1590.

Pavan V, Hall N, Valdes P, Blackburn M. 1999. The importance of moisture distribution for the growth and energetics of midlatitude systems. *Ann. Geophys.* **17**: 242–256.

Polvani LM, Esler JG. 2007. Transport and mixing of chemical airmasses in idealized baroclinic life cycles. *J. Geophys. Res.* **112**: D23102.

Ruprecht E, Schröder S, Ubl S. 2002. On the relation between NAO and water vapour transport towards Europe. *Meteorol. Z.* **11**: 395–401.

Schneider T, Smith KL, O'Gorman PA, Walker CC. 2006. A climatology of tropospheric zonal-mean water vapor fields and fluxes in isentropic coordinates. *J. Climate* **19**: 5918–5933.

Shapiro MA, Keyser D. 1990. 'Fronts, jet streams and the tropopause'. In *Extratropical Cyclones: The Erik Palmén Memorial Volume*. American Meteorological Society: Boston; pp 167–191.

Sinclair VA, Gray SL, Belcher SE. 2008. Boundary-layer ventilation by baroclinic life cycles. *Q. J. R. Meteorol. Soc.* **134**: 1409–1424.

Sinclair VA, Gray SL, Belcher SE. 2010. Controls on boundary-layer ventilation: Boundary-layer processes and large-scale dynamics. *J. Geophys. Res.* **115**: D11107.

Stohl A, Forster C, Sodemann H. 2008. Remote sources of water vapour forming precipitation on the Norwegian west coast at 60°N – a tale of hurricanes and an atmospheric river. *J. Geophys. Res.* **113**: D05102.

Thorncroft CD, Hoskins BJ, McIntyre ME. 1993. Two paradigms of baroclinic-wave life-cycle behaviour. *Q. J. R. Meteorol. Soc.* **119**: 17–55.

Trenberth KE, Stepaniak DP. 2003. Covariability of components of poleward atmospheric energy transports on seasonal and interannual time-scales. *J. Climate* **16**: 3691–3705.

Wernli H. 1997. A Lagrangian-based analysis of extratropical cyclones. II: A detailed case-study. *Q. J. R. Meteorol. Soc.* **123**: 1677–1706.

Wernli H, Fehlmann R, Lüthi D. 1998. The effect of barotropic shear on upper-level induced cyclogenesis: Semigeostrophic and primitive equation numerical simulations. *J. Atmos. Sci.* **55**: 2080–2094.

Yin JH. 2005. A consistent poleward shift of the storm tracks in simulations of 21st century climate. *Geophys. Res. Lett.* **32**: L18701.

